



Size-dependent of compression yield strength and deformation mechanism in titanium single-crystal nanopillars orientated [0001] and [11 $\bar{2}$ 0]

Junqiang Ren, Qiaoyan Sun, Lin Xiao^{*}, Xiangdong Ding, Jun Sun

State Key Laboratory for Mechanical Behaviour of Materials, Xi'an Jiaotong University, Xi'an, Shaanxi 710049, PR China

ARTICLE INFO

Article history:

Received 14 April 2014

Received in revised form

4 July 2014

Accepted 9 July 2014

Available online 27 July 2014

Keywords:

Molecular dynamics simulation

Size effect

Titanium

Dislocations

Surface effect

ABSTRACT

Different size effects and deformation mechanisms are revealed in α -titanium (Ti) single crystal nanopillars orientated for [11 $\bar{2}$ 0] and [0001] based on molecular dynamics simulations. The strength–size relationship changes from “smaller is stronger” to “smaller is much weaker” when the width of nanopillars reduces from 19 nm to 3 nm. The “smaller is much weaker” is attributed to that the surface effect caused by a thermal vibration of surface atoms leads to the initiation and growth of surface dislocations.

© 2014 Elsevier B.V. All rights reserved.

1. Introduction

Plastic deformation behavior of titanium and its alloys in micron- and sub-micron scales has attracted a considerable research interest so far [1–5]. It has been widely accepted that the sample size may exert significant influence on mechanical properties of materials in this scale. Direct experimental observation revealed the dependence of yield strength on sample size in hexagonal-close packed (hcp) single crystals. In this scale, the critical resolved shear stresses and deformation mechanisms are sensitive to the specimen size. Yu et al. [1] studied the size effect of Ti–5% Al single crystal on deformation twinning. It was reported that the twinning stress significantly increased when the pillar diameter decreased to 1 μ m below where twinning deformation completely disappeared and was replaced by dislocation slip. Sun et al. [5] investigated mechanical properties of [11 $\bar{2}$ 0]-oriented Ti submicro-pillars with effective diameter from 0.3 μ m to several microns under uniaxial compression. A pronounced size effect was observed and approximate 16% of the theoretical strength was achieved in Ti when the pillar diameter reduced to 300 nm. However, Jin et al. [6] reported that mechanical strengths of sub-micron columnar cadmium (Cd) approached the theoretical strength of Cd when the Cd structure size reduced to 0.1 μ m. Both Byer [7] and Lilleodden et al. [8] observed pyramidal and $\langle c \rangle$ type

dislocation rather than twins in the deformed magnesium (Mg) single-crystal pillars orientated for [0001] with approximate size of 2–10 μ m. In comparison, Ye et al. [9] reported twinning in sub-micron Mg and Mg–0.2Ce alloy pillars using in situ transmission electron microscopy (TEM) compression testing. “smaller is stronger” was displayed.

A great deal of work has been concentrated on “smaller is stronger” size effect [10]. However, recently, “smaller is much weaker” has been proposed in the nanoscale [11–13]. Schiøtz et al. [12] reported an inverse Hall–Petch relationship in nanocrystal copper using molecular dynamics simulation. The strength exhibits the maximum at a grain size of 10–15 nm. Tian et al. [11] reported that strength–size relationship changed from “smaller is stronger” to “smaller is much weaker” in single-crystal Tin (Sn) samples, when the sample size reduced from 450 nm to 130 nm. In our previous work [13], the “smaller is much weaker” has also been predicted in Ti single-crystal nanopillars orientated for double prismatic slips according to molecular dynamics simulations. These results indicate that there is a transition of strength–size effect as the size decreases. In comparison with highly symmetric cubic metals, the plastic deformation in hcp metal is anisotropic. In particular, the influence of crystallographic orientation on the size effect and the deformation mechanisms of hcp metal nanopillar remain unclear.

MD results show that grain boundary sliding dominates plastic deformation when the grains size is less than the critical size in nanocrystalline copper [12] and [0001] textured nanocrystalline Zr [14]. Compared with grain boundary, free surface has the less

^{*} Corresponding author. Tel.: +86 29 82668614; fax: +86 29 82663453.

E-mail address: lxiao@mail.xjtu.edu.cn (L. Xiao).

constraint and therefore even the larger diffusivity than the interior of crystal. Experimental results demonstrated that diffusional deformation replaced the disclative plasticity as the dominant deformation mechanism in single crystal Sn samples [11]. As the sample dimension decreases to the nanoscale, the free surface can play an important role in dislocation nucleation [15–17]. Frank-Read-like sources are no longer active; plasticity should be surface dominated [18]. Weinberger et al. [19] uncovered the fundamental differences in deformation behavior between face-centered cubic (fcc) and body-centered cubic (bcc) nano-pillars using MD and dislocation dynamics (DD) simulations. They suggested that the screw dislocations in bcc metals have the relative lower mobility than those in hcp metal. The results were also experimentally observed by Greer et al. and Brinckmann et al. [20,21]. Dislocation nucleation mechanism from the free surface was determined via MD simulations by Zhu et al. [22], who developed a framework to describe the probabilistic nature of dislocation nucleation from surfaces. Diao et al. [15] has demonstrated that surface stresses alone caused gold nanowire to transform from fcc structure to the body-centred-tetragonal (bct) structure. The surface stress can be regarded as the driving force for the phase transformation, reorientation and the yield strength asymmetry [16]. This phenomenon has also demonstrated in the bcc nanowires by Li et al. [23] and Cao et al. [24]. However, previous works mainly focus on fcc and bcc materials. Little work is on the hcp structure.

The purpose of this work is to characterize the influences of sample size and crystallography orientation on the ultimate strength and underlying deformation mechanisms in hcp Ti nanopillar using the MD simulation.

2. Simulation method

We investigated the structure and mechanical properties of single-crystalline nanopillars using MD simulations with the many-body potential of the Finnis–Sinclair type by Ackland [25]. The Finnis–Sinclair many body potential is suitable for describing the defect evolution in Ti single crystals during loading, since it describes reasonably well physical properties of Ti according to the calculation results of the energies of point defects, surfaces, elastic constants and planar faults in the equilibrium structures. The potential has been successfully employed to describe a variety of defects, surfaces, twin boundary structures, and atomic interaction in Ti [26,27].

The initial nanopillars with different crystallographic orientations were created out of a bulk hcp metal crystal. The computational supercell had the dimensions x – $[1\bar{1}00]$, y – $[11\bar{2}0]$ and z – $[0001]$, with the free surface boundary condition. In this study, we focused on $[11\bar{2}0]$ and $[0001]$ oriented rectangle cross-section nanopillars. The height-to-width ratio of all of the nanopillars considered for the simulations was 2:1 and the dimension varying from 3 nm to 19 nm. The single crystal nanopillars were compressed along $[11\bar{2}0]$ and $[0001]$, respectively. The conjugate gradient algorithm was used to obtain an equilibrium state before loading. The time step was 1.0 fs. A Nose–Hoover thermostat was used to maintain a constant temperature of 300 K during deformation in canonical ensemble, (constant atom number, volume and temperature, NVT). The strain rate during loading was $1 \times 10^8 \text{ s}^{-1}$. Common neighbor analysis (CNA) [28] was used to distinguish a variety of defects and atoms in (fcc-like) stacking faults from hcp-coordinated atoms. MD calculations were conducted with the software LAMMPS [29] and snapshots of simulation result were processed by AtomEye [30].

3. Results

3.1. Size effect of yield stress

In order to understand the size effects of yield stress of Ti nanopillar, a series MD simulation have been performed with various nanopillar widths subjected to uniaxial compression along $[11\bar{2}0]$ and $[0001]$ orientation, respectively. The yield stress is defined as the maximum uniaxial compressive stress. The snapshots of the compressive deformation are captured to understand the yield mechanism of nanopillar. For viewing inner defects, the front and back surface and hcp atoms are not shown. The variety of nanopillar shape and the evolution of interior defects are snapped from different perspectives. The atoms were colored according to common neighbor analysis (CNA [28]). Hcp atoms were colored light blue; fcc atoms were colored with dark blue; defect and surface atoms were colored with red.

Fig. 1 shows the uniaxial compressive yield stress as a function of the width. The Ti $[0001]$ -oriented nanopillar with the width of 12 nm yields at a stress of about 7.6 GPa, and the yield stress declines to 6.39 GPa for the nanopillar width of 19 nm. It means that an inverse linear relationship is displayed between the yield stress and the sample widths when the pillar width is larger than the critical width of 12 nm. In other words, the conventional size effect, “smaller is stronger”, is demonstrated above the critical width of 12 nm. However, when the nanopillar width is less than 12 nm, the yield stress continuously decreases from 7.16 GPa for the 11-nm nanopillar to 6.17 GPa for the 5-nm-wide nanopillar; thereby they demonstrate an inverse size effect, i.e. the relationship between the yield stress and the pillar width displays proportional when the width is less than 12 nm. When the Ti $[0001]$ -oriented nanopillars width reduces from 19 nm to 5 nm, the relationship between yield stress and the pillar width changes from “smaller is stronger” to “small is much weaker” [11]. The same tendency is also displayed in the compressed Ti $[11\bar{2}0]$ -oriented nanopillars [13]. In comparison, the critical width of the $[11\bar{2}0]$ -oriented nanopillar is 7 nm, which is smaller than the $[0001]$ -oriented nanopillar. According to the linearly regression results, the critical widths of the $[0001]$ -oriented nanopillar and the $[11\bar{2}0]$ -oriented nanopillar are 12.8 nm and 7.0 nm, respectively.

3.2. Deformation mechanism

Fig. 2 shows snapshots of dislocation structure in the deformed Ti $[11\bar{2}0]$ nanopillars, when the width of pillars is less than 7 nm. The dislocations with Burgers vector \mathbf{b}_1 and \mathbf{b}_2 initiated and grew

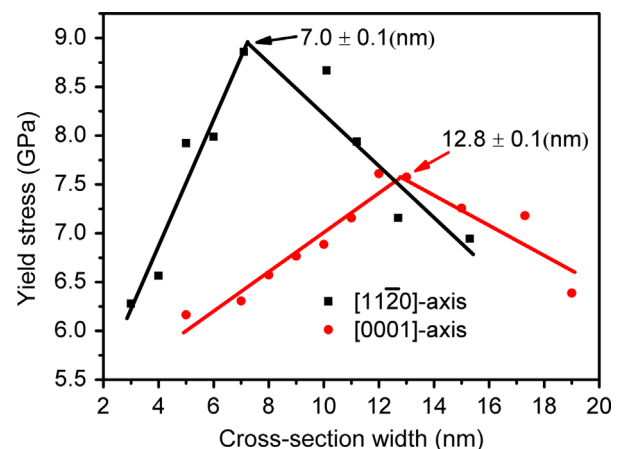


Fig. 1. The uniaxial compressive yield stress as a function of the width for the $[11\bar{2}0]$ -oriented nanopillars and the $[0001]$ -oriented nanopillars.

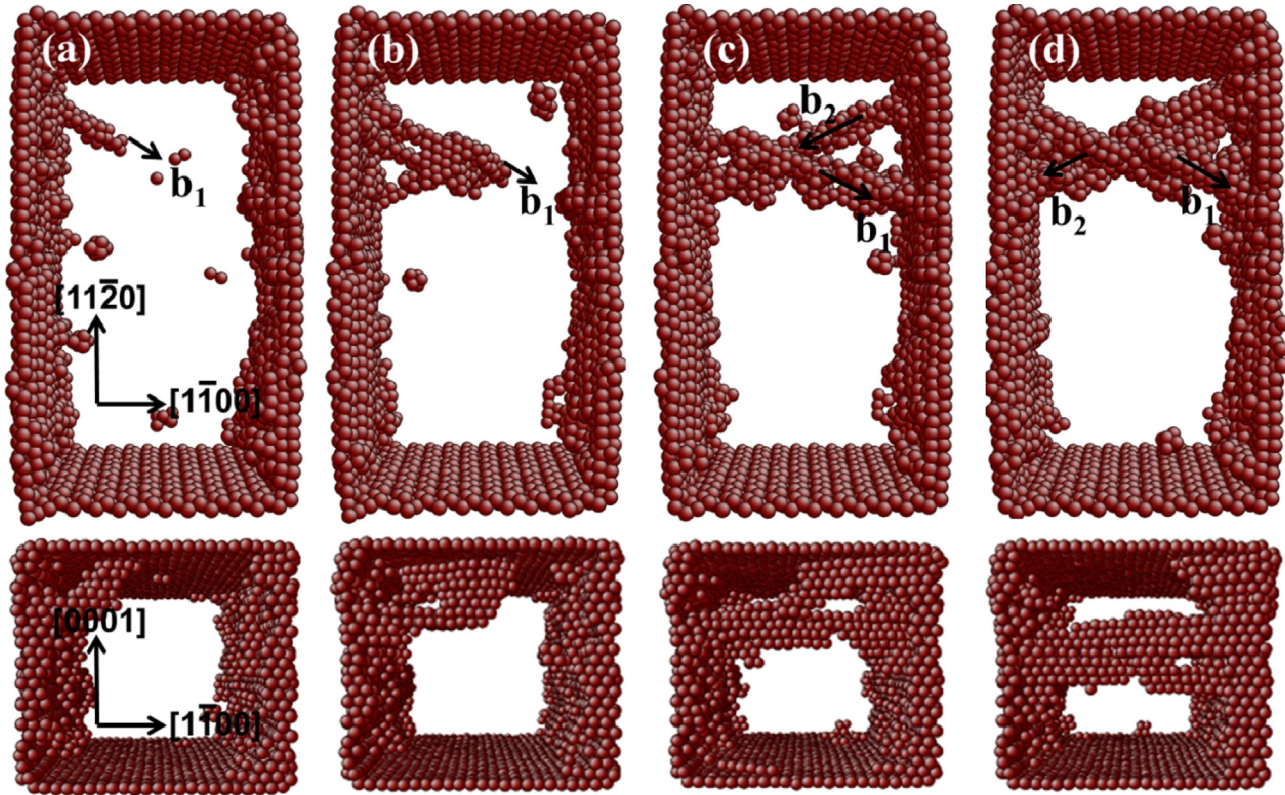


Fig. 2. Snapshots of $[11\bar{2}0]$ -oriented Ti nanopillar under compressive loading for pillars with the width less than 7 nm. The \mathbf{b}_1 and \mathbf{b}_2 are the Burgers vectors of dislocations.

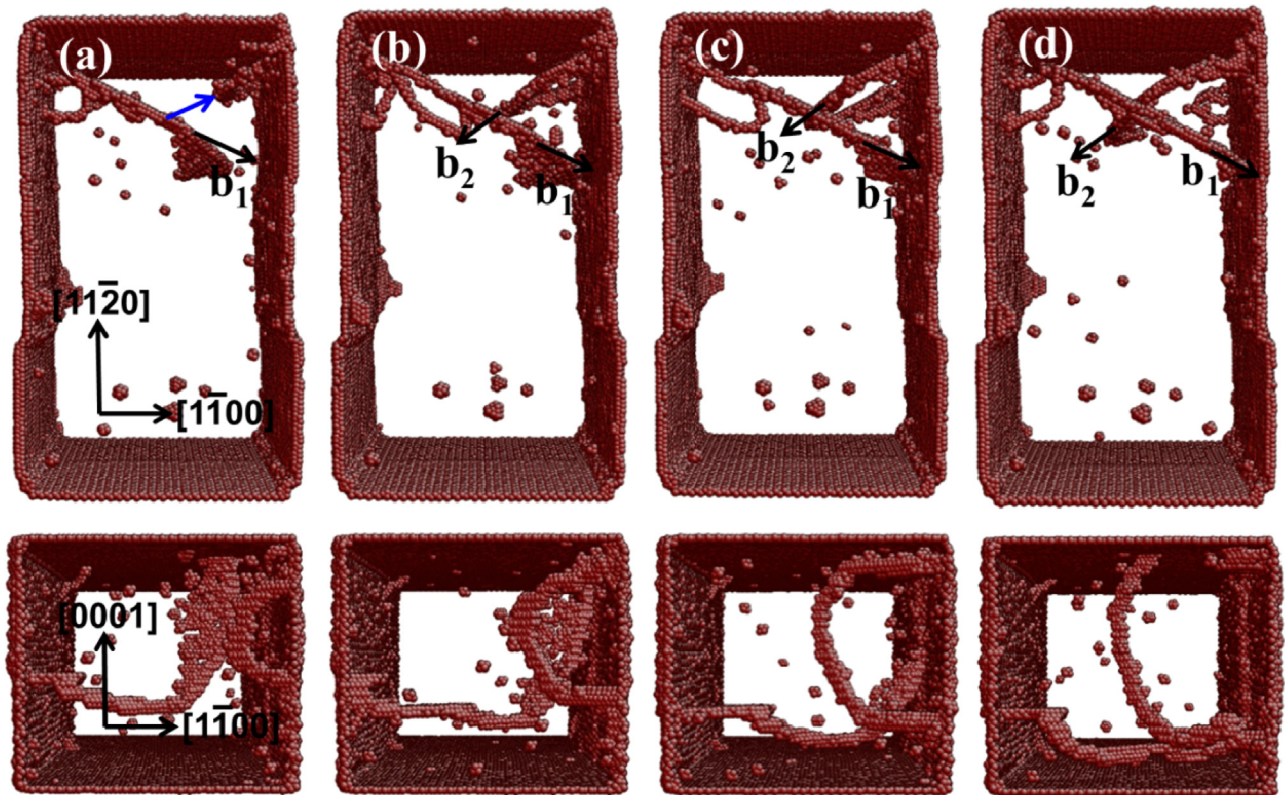


Fig. 3. Snapshots of $[11\bar{2}0]$ -oriented Ti nanopillar under compressive loading when the pillar width is larger than 7 nm. The \mathbf{b}_1 and \mathbf{b}_2 indicate the Burgers vectors of dislocations.

from the free surfaces. Two groups of dislocations propagated along $(\bar{1}010)$ $[1\bar{2}10]$ and $(0\bar{1}10)$ $[\bar{2}110]$, respectively. In difference with dislocation half loops formed in the pillars large than 7 nm,

dislocations in the form of planar dislocation bundles initiated and propagated from the surface, as shown in Fig. 2(a–d). The Burgers vectors are perpendicular to these dislocation lines, as shown in

Fig. 2. Thus, the dislocations were determined to be main edge-type dislocations.

Fig. 3 illustrates the process of dislocations movement during deformation, when the Ti [1120]-oriented nanopillar width is larger than 7 nm. The dislocations nucleation site is indicated by an arrow in Fig. 3(a). It is demonstrated that dislocations nucleate and grow from the top left corner along $(\bar{1}010)$ $[1\bar{2}10]$ and $(0\bar{1}10)$ $[2\bar{1}10]$ double prismatic slip planes with an angle of 120° as the plastic deformation progresses. The similar results were experimentally observed by Sun et al. [5] in the Ti single crystal pillar with the size of 0.3–3 μm . This indicates that double prismatic slips with Burger vectors $\mathbf{b}_1 = a/3 [1\bar{2}10]$ and $\mathbf{b}_2 = a/3 [2\bar{1}10]$ were activated under compression along $[11\bar{2}0]$. A group of dislocations in the form of half loops initiated and propagated from the surface, as shown in Fig. 3(a–d). This indicates that the multiplication and growth of mixed types of dislocations took place inside pillars. Finally, dislocations disappear on the surface.

The snapshots of the Ti [0001]-oriented nanopillars deformation are shown in Figs. 3 and 4. No compression twins were observed at various widths. This is consistent with microcompression experimental and MD simulation results in the magnesium [7,8,31] and Ti–5% Al [1] (0001) single crystal. $\{10\bar{1}2\}$ and $\{10\bar{1}1\}$

twins can be activated under the c -axis tension, while compression twins will not occur when the c/a ratio of the hcp metal is less than $\sqrt{3}$ [31,32]. MD simulation of compression deformation shows that the pyramidal slip dominates compression behavior in the nanoscale. The initial compressive yielding was found to be mediated by the nucleation and propagation of the Shockley partial dislocations with the Burgers vector of $1/2\langle 10\bar{1}2 \rangle$. When the width of nanopillar is 9-nm, the partial dislocation initiated from the corner and the surface at a compressive strain of 4.4%, as is indicated by a blue arrow in Fig. 4(a). The simulation reveals that two dislocations simultaneously nucleated and grew in the corner of pillar along the $(10\bar{1}1)$ and $(\bar{1}101)$ pyramidal slip planes (Fig. 4(a–g)). The Burgers vectors were determined to be $\mathbf{b}_1 = 1/2.1/2 [10\bar{1}2]$ and $\mathbf{b}_2 = 1/2.1/2 [0\bar{1}12]$ based on the crystallographic analysis [33]. The trailing partial dislocations with the Burger vectors $\mathbf{b}_3 = 1/2.1/2 [10\bar{1}2] + 1/2.1/3 [1\bar{2}10]$ and $\mathbf{b}_4 = 1/2.1/2 [0\bar{1}12] + 1/2.1/3 [2\bar{1}10]$ nucleated from the corner and then combined to form the unit dislocations $\mathbf{b}_5 = 1/3\langle 2\bar{1}13 \rangle$ and propagated on the $(10\bar{1}1)$ and $(\bar{1}101)$ slip planes. This indicates that pyramidal slips $(10\bar{1}1) [2\bar{1}13]$ and $(\bar{1}101) [1\bar{2}13]$ were activated under compression along $[0001]$ direction. Finally, these dislocations were absorbed by surface, as indicated by the arrows in Fig. 4(f–g). Strong dislocation

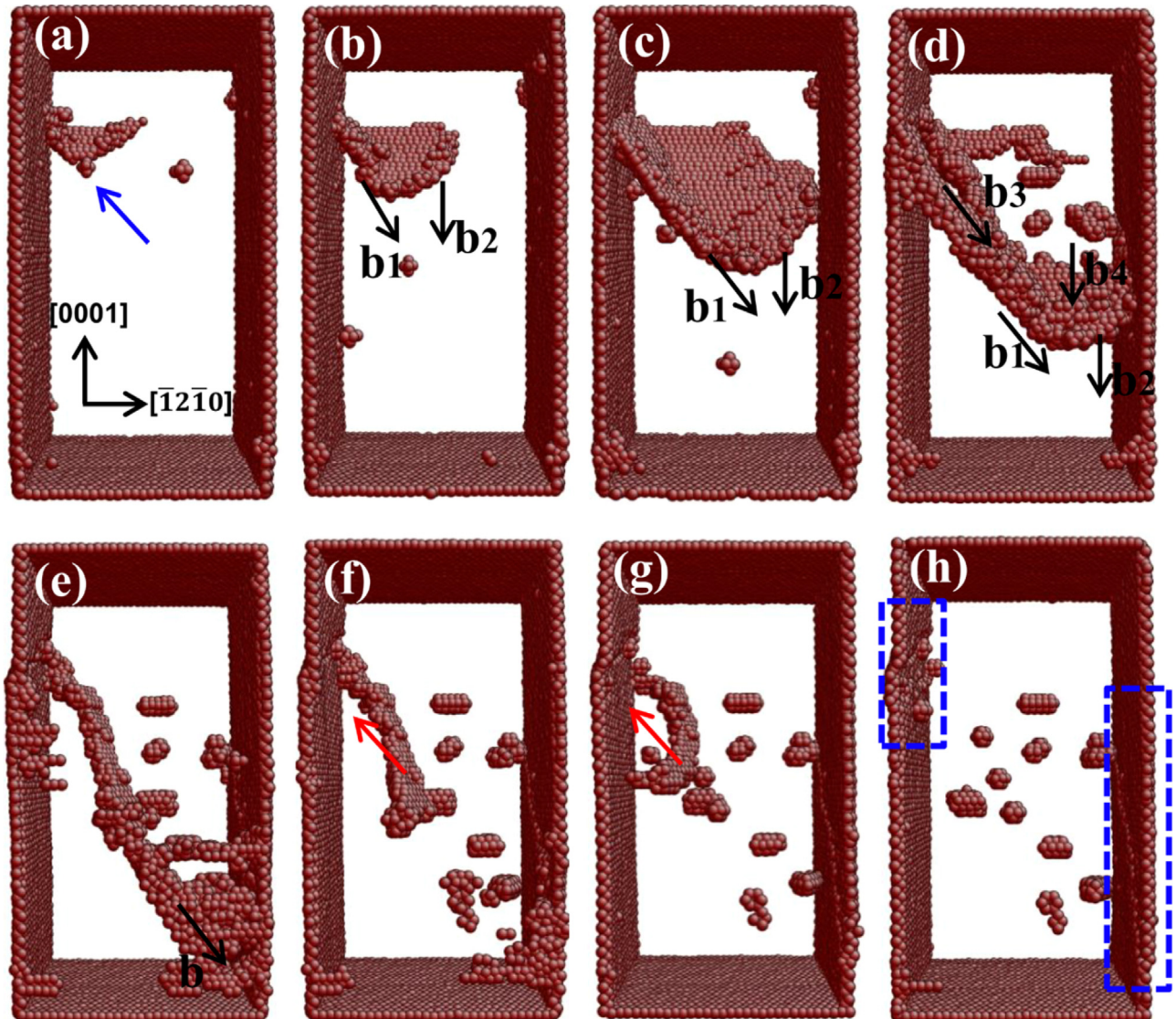


Fig. 4. Snapshots of [0001]-oriented Ti nanopillar under compressive loading for pillars with the width less than 12 nm. The \mathbf{b} and \mathbf{b}_1 – \mathbf{b}_4 indicate the Burgers vectors of the unit dislocation and the partial dislocations, respectively. (For interpretation of the references to colour in this figure, the reader is referred to the web version of this article.)

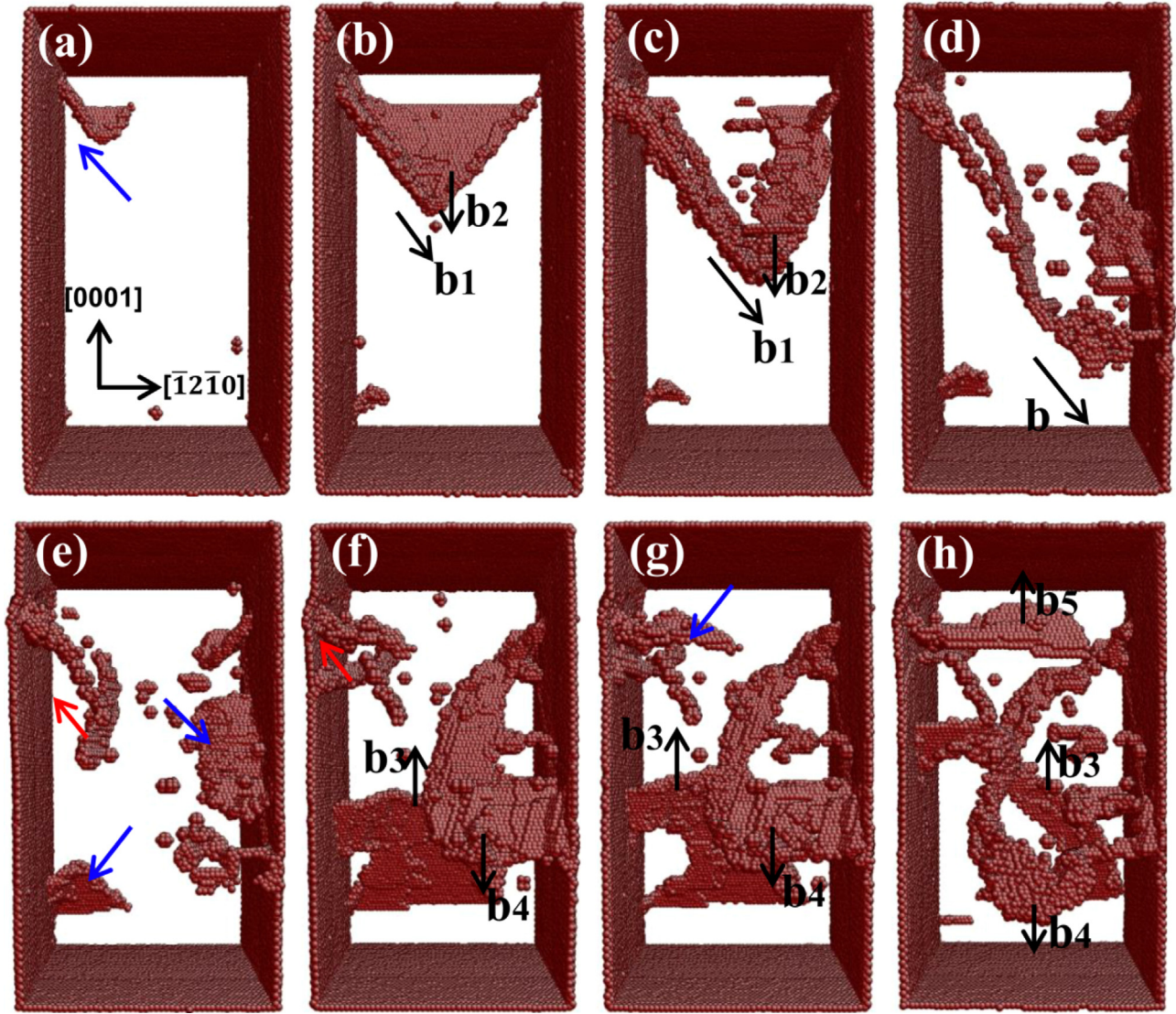


Fig. 5. Snapshots of [0001]-oriented Ti nanopillar under compressive loading when the pillar width is larger than 12 nm. The **b** and **b₁–b₅** indicate the Burgers vectors of the unit dislocation and the leading partial dislocations, respectively. (For interpretation of the references to colour in this figure, the reader is referred to the web version of this article.)

interactions did not happen due to the small sample size and easily escape of dislocations to the nearby surfaces. As a result, slip steps on the surface and defect cluster inside the pillar were produced as indicated by two blue dotted squares in Fig. 4(h). The sequential emission of the leading and trailing partial dislocations was observed in the pillar when the width was greater than 12 nm. Fig. 5(a–h) illustrates typical snapshots of the deformed 15-nm-wide pillar along the (10 $\bar{1}$ 0) crystal plane. The dislocation process can be expressed as

$$\frac{1}{2}[10\bar{1}2] + \frac{1}{6}[1\bar{2}10] \rightarrow \frac{1}{3}[2\bar{1}\bar{1}\bar{3}]$$

$$\frac{1}{2}[0\bar{1}1\bar{2}] + \frac{1}{6}[2\bar{1}\bar{1}0] \rightarrow \frac{1}{3}[1\bar{2}1\bar{3}]$$

The trailing partial dislocation follows the leading one and creates the observed full dislocation. Because of the high stored elastic strain energy, once the plastic yielding starts, the shear can be clearly observed in a plane representation, but no structural defect is formed in the slip region after the pyramidal slip, leaving multiple slip lines on the free surfaces and a dislocation-free state inside the pillar. These surface defects are much localized stress

concentration sites, and the dislocation nucleation can occur more easily when the width of pillar is greater than 12-nm. The partial dislocations nucleated in these potential dislocation nucleation sites, as indicated by the blue arrows in Fig. 5(e and g).

No strain hardening was observed at different widths of pillars subjected to uniaxial compression along the [11 $\bar{2}$ 0] and [0001] orientation at 300 K. This indicates the lack of dislocation storage mechanisms. As shown in Figs. 2 and 4, when a small amount of dislocations nucleated, it rapidly glided away from its nucleation site, and escaped the pillar through its surfaces. As shown in Fig. 5, several dislocations nucleated from surface within a time shorter than necessary for previous dislocations elimination, these dislocations tend to glide into the interior of pillar. But all of the dislocations eventually were absorbed by their surfaces.

3.3. Size effect of strengthen coefficient

According to homogenous nucleation theory, dislocation loops could nucleate in the perfect crystal when the radius of a potential nucleus exceeds the critical value, r_c . The resolved shear stress

needed to nucleate a dislocation loop can be expressed as [34]

$$\tau_c = \frac{Gb}{2\pi r_c} \quad (1)$$

where G is the shear modulus, b is Burgers vector. Dan Mordehai et al. [35] calculated the critical compressive stress σ_c , which is defined as the stress when the radius of dislocation loops expands to the critical radius, r_c , on the sample surface:

$$\sigma_c \sim R^{-n} \quad (2)$$

where R is the microparticle size, n is the exponent in the power law decay of the yield stress with increasing the nanopillar width. When the pillar width is larger than twice critical radius r_c , dislocation loop will be a stable nucleus and grow in the form of arc-shaped dislocation during compressive loading. As a result, different deformation mechanisms will be activated as the pillar width decreases. The relationship between the compressive stress and the nanopillar width R in dual-logarithm coordinates is shown in Fig. 6(a). The MD results suggest that the exponent $n=0.33 \pm 0.097$ for the [0001]-oriented nanopillar, which is nearly consistent with $n=0.35 \pm 0.09$ for [11 $\bar{2}$ 0]-oriented nanopillar.

The yield stress increases with decreasing width when the width of nanopillar exceeds the critical width. In comparison, Fig. 6(b) reveals that, the exponent n for [11 $\bar{2}$ 0]-oriented nanopillar is -0.41 ± 0.065 smaller than -0.22 ± 0.037 for the [0001]-oriented nanopillar when the nanopillar width is less than the critical width. The value of exponent n is negative, which

indicate that an inverse size effect, i.e. “smaller is much weaker” is displayed. Although the general trend of decreasing yield strength with decreasing pillar width is consistent, crystallography orientation effects on exponent n cannot be ignored. The yield strength of [0001]-oriented nanopillar is obviously smaller than [11 $\bar{2}$ 0]-oriented. The critical width of the [0001] nanopillar (12 nm) is greater than that of the [11 $\bar{2}$ 0] nanopillar (7 nm).

4. Discussion

Dislocation slip and twinning are primary plastic deformation modes of crystalline materials. As the sample dimension decreases to the nanoscale, where Frank-Read-like source is no longer active, plastic deformation transfers to be dominated by the surface due to the high surface-to-volume ratio [36]. Dislocations easily escape from the free surface. Consequently, the crystal becomes starved of dislocation [37], resulting in a “dislocation-starved” state [35]. This phenomenon was demonstrated with in situ TEM compressions of Ni pillars [38]. The nanopillars in our MD simulations were originally dislocation-free. This is the same as mobile-dislocation-free in the experiments. Therefore, the yield point is determined by first dislocation nucleation. The size effect should be associated with the probability of dislocation nucleation on the free surface. A model is used for dislocation loop nucleation in the elastic strain field.

In previous MD simulations work, we predicted that the inverse size effect is attributed to the surface effect caused by a thermal vibration of the surface atoms [13]. The surface effect plays an important role in controlling the nucleation and growth of the dislocation in the nanopillars [39]. The slip would nucleate on the surface when the thermal vibrations reached the maximum. The relation between yield stress and thermal strain can be expressed as [39]

$$\sigma_y = f(\varepsilon_c - \varepsilon_{\text{therm}}) \quad (3)$$

where σ_y is yield stress, ε_c is critical atomic strain of slip nucleation, and $\varepsilon_{\text{therm}}$ is thermal strain. The potential energy of surface atom increases with the decrease of width, thermal expansion pushes neighboring atoms further apart and weakens their mutual interaction. Furthermore, the large activation entropy on the surface is attributed to the weak atomic bonding caused by thermal expansion and thermal softening [40], which results in crystallographic planes to be easier to shear and significantly reduces the free energy barrier for dislocation nucleation.

As shown in the above results (Fig. 6), the reason why the critical width and the strengthen coefficient are different under two orientations when the width of nanopillar is less than the critical width (Fig. 6) is that the {0001} surfaces in hcp metals have the lowest energy among all surfaces. For example, the calculated surface energy for {0001} and {11 $\bar{2}$ 0} are 993 mJ m^{-2} and 1187 mJ m^{-2} , respectively [24]. This difference in surface energy causes the <11 $\bar{2}$ 0>-oriented nanopillar to have a lower energy and to be more stable compared with the <0001>-oriented nanopillar.

The potential energy differences of surface atoms as a function of Ti nanopillar width between these two orientation nanopillars are described in Fig. 7. The potential energy of the two orientation nanopillars is computed after the system reaches their equilibrium states through conjugate gradient energy minimization using molecular statics [41]. The difference of potential energy primarily results from the different energy density between {0001} and {11 $\bar{2}$ 0} surfaces. The average potential energy per atom rapidly increases with decreasing width for each orientation because the smaller nanopillars have the extreme high surface-to-volume ratios when the sample size is less than critical width. The [11 $\bar{2}$ 0]-oriented nanopillar always have the lower energy levels

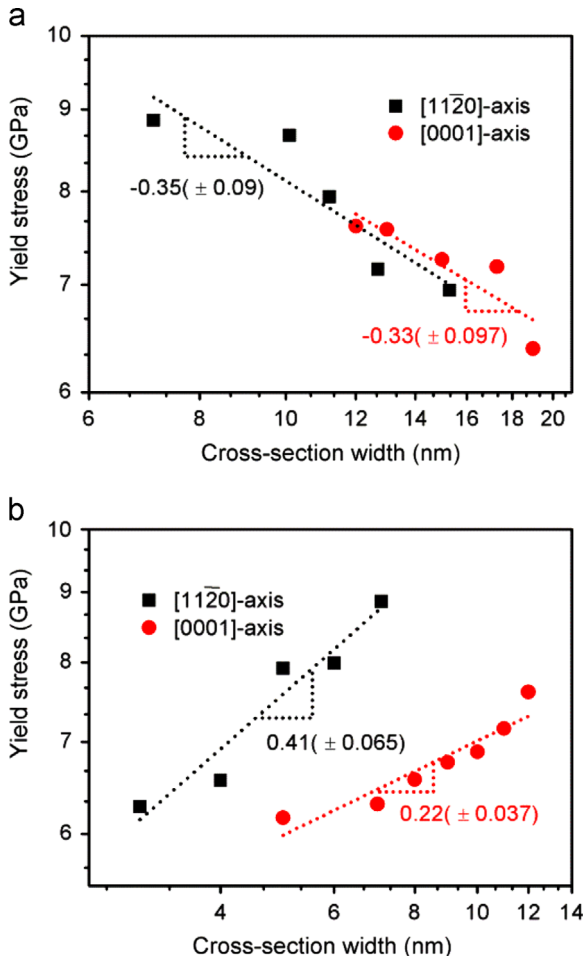


Fig. 6. The dependence of the compressive stress on the various widths: (a) greater than critical width and (b) less than critical width.

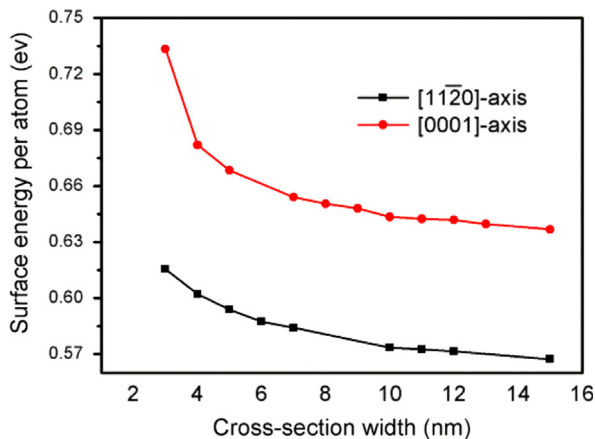


Fig. 7. The variation of average surface energy per surface atom as a function of the pillar width.

compared with the [0001]-oriented nanopillar. The MD simulation results show that the difference of average potential energy per surface atom is obvious.

This work mainly focuses on the influence of nanopillar size on the deformation mechanism and yield stress. The nanopillar was deformed at a constant temperature of 300 K and a strain rate of $\dot{\epsilon} = 1 \times 10^8 \text{ s}^{-1}$. The strain rate applied in MD simulation is a few orders of magnitude faster than those in experiments, such as $\dot{\epsilon} = 5 \times 10^3 \text{ s}^{-1}$ [5]. In fact, the strain rate has a significant effect on the flow stress. Zhu et al. [22] have demonstrated that small activation volume led to a sensitive strain rate dependence of the nucleation stress. Fan et al. [42] have presented a constitutive model to describe the variation of plastic flow stress with strain rate. MD simulations provide a qualitative understanding of the deformation behavior observed in the experiment [35,43,44]. However, special attention should be paid to interpret experiments using the MD simulations. Recent simulation work performed by Fan et al. [45] demonstrated that the same dislocation–obstacle interaction unit could lead to entirely different mechanisms at different strain rates. Therefore, the further investigation is essential on the variety of deformation mechanism and yield stress in the larger ranges of strain rates and the wider ranges of deformation conditions in the future.

5. Conclusion

Molecular dynamics simulations have been used to study the effect of sample size and crystallographic orientation on the strength of Ti single-crystal nanopillars. The defect-free nanopillars yield is controlled by the nucleation and propagation of dislocations from the free surface. Based on this study, the following conclusions can be drawn:

- (1) The conventional size effect “smaller is stronger” trend eventually switches to an inverse size effect, i.e. “smaller is much weaker” with decreasing nanopillar width for both [0001]-orientated and [1120]-oriented nanopillar subjected to compress, when the nanopillars width was reduced from 19 nm to 3 nm. This transition is attributed to the surface stress and thermal vibration.
- (2) The critical width for the [0001]-oriented and [1120]-oriented nanopillar are 7.0 and 12.8 nm, respectively. The difference in

the critical width is attributed to the difference of the surface potential energy.

- (3) The plasticity of the [1120]-oriented nanopillars is predominantly produced by the edge dislocation lines, which nucleate on the surface when the pillar width is less than critical width. The pyramidal $\langle c+a \rangle$ slip is the main deformation mechanism in all [0001]-oriented nanopillars under compression loading. No compression twins were observed.

Acknowledgments

This project was supported by the National Natural Science Foundation of China (51271136, 51071118, 51171140 and 50831004) the 973 Programme of China (2010CB631003), and the 111 Project of China (B06025).

References

- [1] Q. Yu, Z.W. Shan, J. Li, X.X. Huang, L. Xiao, J. Sun, E. Ma, *Nature* 463 (2010) 335–338.
- [2] J.C. Gong, A. Wilkinson, *Acta Mater.* 59 (2011) 5970–5981.
- [3] Q. Yu, S.Z. Li, A.M. Minor, J. Sun, E. Ma, *Appl. Phys. Lett.* 100 (2012) 063109.
- [4] Q. Yu, J. Sun, J.W. Morris Jr., A.M. Minor, *Scr. Mater.* 69 (2013) 57–60.
- [5] Q. Sun, Q. Guo, X. Yao, L. Xiao, J.R. Greer, J. Sun, *Scr. Mater.* 65 (2011) 473–476.
- [6] S. Jin, M.J. Burek, N.D. Evans, Z. Jahed, T.Y. Tsui, *Scr. Mater.* 66 (2012) 619–622.
- [7] C.M. Byer, B. Li, B. Cao, K.T. Ramesh, *Scr. Mater.* 62 (2010) 536–539.
- [8] E. Lilleodden, *Scr. Mater.* 62 (2010) 532–535.
- [9] J. Ye, R.K. Mishra, A.K. Sachdev, A.M. Minor, *Scr. Mater.* 64 (2011) 292–295.
- [10] J.R. Greer, J.T.M. De Hosson, *Prog. Mater. Sci.* 56 (2011) 654–724.
- [11] L. Tian, J. Li, J. Sun, E. Ma, Z.W. Shan, *Sci. Rep.* 3 (2013) 2113.
- [12] J. Schiøtz, K.W. Jacobsen, *Science* 301 (2003) 1357–1359.
- [13] J. Ren, Q. Sun, L. Xiao, X. Ding, J. Sun, *Philos. Mag. Lett.* 10 (2013) 583–590.
- [14] C.J. Ruestes, G. Bertolino, M. Ruda, D. Farkas, E.M. Bringa, *Scr. Mater.* 71 (2014) 9–12.
- [15] J. Diao, K. Gall, M.L. Dunn, *Nat. Mater.* 2 (2003) 656–660.
- [16] J. Diao, K. Gall, M.L. Dunn, *Nano Lett.* 4 (2004) 1863–1867.
- [17] E. Rabkin, H.S. Nam, D.J. Srolovitz, *Acta Mater.* 55 (2007) 2085–2099.
- [18] J.R. Greer, W.D. Nix, *Phys. Rev. B* 73 (2006) 245410.
- [19] C.R. Weinberger, W. Cai, *Proc. Natl. Acad. Sci. USA* 105 (2008) 14304–14307.
- [20] J.R. Greer, C. Weinberger, W. Cai, *Mater. Sci. Eng. A* 493 (2008) 21–25.
- [21] S. Brinckmann, J.Y. Kim, J.R. Greer, *Phys. Rev. Lett.* 100 (2008) 155502.
- [22] T. Zhu, J. Li, A. Samanta, A. Leach, K. Gall, *Phys. Rev. Lett.* 100 (2008) 025502.
- [23] S. Li, X. Ding, J. Deng, T. Lookman, J. Li, X. Ren, J. Sun, A. Saxena, *Phys. Rev. B* 82 (2010) 205435.
- [24] A. Cao, J. Appl. Phys. 108 (2010) 113531.
- [25] G.J. Ackland, *Philos. Mag. A* 66 (1992) 917–932.
- [26] G.J. Ackland, S.J. Wooding, D.J. Bacon, *Philos. Mag. A* 71 (1995) 553–565.
- [27] A. Serra, D.J. Bacon, *Acta Metall.* 43 (1995) 4465–4481.
- [28] J.D. Honeycutt, H.C. Andersen, *J. Phys. Chem.* 91 (1987) 4950–4963.
- [29] Z. Yang, Z. Lu, Y.P. Zhao, *J. Appl. Phys.* 106 (2009) 023537.
- [30] J. Li, *Model. Simul. Mater. Sci. Eng.* 11 (2003) 173.
- [31] Y. Guo, X. Tang, Y. Wang, Z. Wang, S. Yip, *Acta Metall. Sin. (Engl. Lett.)* 26 (2013) 75–84.
- [32] M.H. Yoo, *Metall. Trans. A* 12 (1981) 409–418.
- [33] B. Li, E. Ma, *Philos. Mag.* 89 (2009) 1223–1235.
- [34] D. Hull, D.J. Bacon, *Introduction to Dislocations*, fourth ed., Butterworth-Heinemann, Oxford, 2001.
- [35] D. Mordehai, S.W. Lee, B. Backes, D.J. Srolovitz, W.D. Nix, E. Rabkin, *Acta Mater.* 59 (2011) 5202–5215.
- [36] J.R. Greer, W.D. Nix, *Phys. Rev. B* 73 (2006) 245410.
- [37] D. Kiener, A.M. Minor, *Acta Mater.* 59 (2011) 1328–1337.
- [38] Z.W. Shan, R.K. Mishra, S.A.S. Asif, O.L. Warren, A.M. Minor, *Nat. Mater.* 7 (2008) 115–119.
- [39] E. Rabkin, D.J. Srolovitz, *Nano Lett.* 7 (2007) 101–107.
- [40] S. Ryu, K. Kang, W. Cai, *Proc. Natl. Acad. Sci. USA* 108 (2011) 5174–5178.
- [41] M.C. Payne, M.P. Teter, D.C. Allan, T.A. Arias, J.D. Joannopoulos, *Rev. Mod. Phys.* 64 (1992) 1045–1097.
- [42] Y. Fan, Y.N. Osetskiy, S. Yip, B. Yildiz, *Phys. Rev. Lett.* 109 (2012) 135503.
- [43] Y. Lu, J. Song, J.Y. Huang, J. Lou, *Adv. Funct. Mater.* 21 (2011) 3982–3989.
- [44] D. Mordehai, M. Kazakevich, D.J. Srolovitz, E. Rabkin, *Acta Mater.* 59 (2011) 2309–2321.
- [45] Y. Fan, Y.N. Osetskiy, S. Yip, B. Yildiz, *Proc. Natl. Acad. Sci.* 110 (2013) 17756–17761.